ORIGINAL PAPER

Low-Temperature Plasma Oxidation of Aluminum by Ar-O_2 Mixtures in a Dielectric-Barrier Discharge Reactor

Claus-Peter Klages[1] · Antje Jung[1] · Meret Leonie Betz[1] · Vitaly Raev[1]

Abstract

Room-temperature growth of oxide layers on aluminum in highly diluted mixtures of oxygen with argon (O_2 molar fractions 20 ppm $\leq x_{O_2} \leq$ 500 ppm, partial pressures 2 Pa $\leq p_{O_2} \leq$ 50 Pa) flowing through a dielectric-barrier discharge (DBD) reactor is studied, including oxidation in the pre- and post-discharge regions (PrD, PoD) adjacent to the main DBD. Three different mechanisms of plasma-enhanced oxidation were found to prevail, depending on the location of the sample: (1) In the close PrD region, up to 1 cm upstream from the discharge, accelerated growth of Al_2O_3 is due to the irradiation of the sample surface by highly energetic (9.8 eV) argon excimer radiation in the presence of O_2. (2) In the remote PoD, a few cm downstream from the DBD, oxidation can largely be attributed to oxygen atoms, with number densities typically between 1 and 5×10^{14} cm^{-3}. Here, analysis in terms of Cabrera–Mott (CM) theory results in CM potentials between -1.5 and -2.1 V. (3) In the DBD itself both O atoms and VUV photons generally play an important role but, under special conditions, an additional oxidation mode can be identified, characterized by a much larger limiting thickness: While, in general, oxide growth by O atoms and/or VUV photons virtually stops at thicknesses X between 5 and 6 nm, much thicker oxide films can be achieved in the downstream region of the main DBD, with thicknesses growing with the length of the DBD zone. Tentatively, we attribute this observation to negative oxygen ions O_m^- ($1 \leq m \leq 3$) accumulating in the gas while passing the reactor. Any direct electrical effects of the discharge process on the oxidation can probably be neglected.

Keywords Dielectric-barrier discharge (DBD) · Aluminum · Plasma oxidation · Oxygen atoms · Vacuum ultraviolet

Introduction

The oxidation of aluminum and its alloys is a topic of continuing practical relevance and scientific interest [1–4]. Apart from the superior corrosion resistance of the oxide layers formed spontaneously on a fresh metal aluminum surface exposed to air, aluminum oxide

✉ Claus-Peter Klages
c-p.klages@tu-braunschweig.de

[1] Institute for Surface Technology, IOT, Technische Universität Braunschweig, Riedenkamp 2, 38108 Braunschweig, Germany

is of interest as an insulating layer for gates of field-effect transistors [5], in Josephson tunnel junctions for qubits in superconducting quantum computers [6], or for resistive-switching memories with metal–insulator-metal (MIM) diodes [7], to mention three applications of current interest. Thermal growth of aluminum oxide on the metal surface at low temperatures, i.e., below about 600 K [8], is generally self-limiting in the sense that the oxide thickness grows relatively fast to a certain thickness beyond which the oxidation rate is much smaller: In 1947, Hass reported oxide growth on evaporated aluminum in air up to a thickness of 4.2 nm within 60 days (5×10^6 s) which was virtually unchanged within the following 60 days [9]. Using X-ray photoelectron spectroscopy (XPS), oxide thicknesses of 3.1 and 3.4 nm, respectively, were measured more recently on mirror-polished (100) and (111) surfaces of Al single crystals, exposed to the open air, virtually not changing within one year (3×10^7 s) [10]. Under controlled laboratory conditions, the thickness which is achieved within typically 10^4 s at 300 K can be tuned via the oxygen partial pressure: from 0.2 nm at 1×10^{-8} Torr to 1.2 nm at 5 Torr [11], while 2.0 nm are obtained at 311 K and 600 Torr O_2 within 6×10^5 s [12].

The theory developed by Cabrera and Mott (CM) [13] explains low-temperature growth of metal oxides by the establishment of a negative electrical potential, the later so-called Cabrera–Mott potential, V_{CM}, by negative charging of oxygen species adsorbed on the surface of the oxide, due to the transfer of electrons from the metal to adsorbed O_2 molecules. The resulting electric field lowers the potential barrier which mobile ions have to overcome in order to be injected into the oxide and/or to drift to the opposing metal/oxide or oxide/gas interface where they recombine with counterions and form new oxide. At present, there is not yet an unequivocal answer to the question what the dominant mobile species is: On one hand there is experimental evidence from electrical 4-point probe measurements that formation of amorphous Al_2O_3 layers on Al(111) at 300 K takes place by outward film growth due to Al^{3+} ion transport from the metal to the oxide/gas interface [14]. This mechanism is frequently assumed by other authors, too [2, 3, 15]. On the other hand, medium-ion scattering studies of oxygen transport and oxidation kinetics of Al(110) were interpreted in terms of oxygen anions as mobile species, transported via migration of oxide network defects [16]. In wet-chemical anodic oxide formation on aluminum, having a similar mechanism like dry oxide formation [17], both, metal cations and oxygen anions are mobile [18]. The possibility that mobile cations and anions play a role in dry oxidation is also considered, e.g., by Ramirez et al. [1]

In order to achieve oxide growth beyond thicknesses in the lower nanometer range and to enable a control of oxide properties, plasma oxidation has been applied in numerous studies since at least the 1960s [19, 20]. Halverson and Cocke reported plasma-assisted oxidation within one hour up to thicknesses twice as large (9 to 11 nm at 340 to 740 K) as thermal thicknesses achieved at the same temperature (4.5 to 5.5 nm) [21]. Aside from several other important publications on oxidation of aluminum by plasmas [22–26], a contribution by Rider et al. [27] deserves special attention in the present context because the experimental results, obtained in low-pressure 125-kHz discharges with areal power densities of less than 0.5 Wcm^{-2} and partial pressures of 10 Pa O_2 (or H_2O) were interpreted in terms of Cabrera–Mott theory. CM parameters X_1 and u were extracted from the data, using Ghez' approximative solution of CM's differential equation for oxide growth. Interestingly, similar $X(t)$ curves and X_1 values were reported as found in this study, see below.

In preliminary combinatorial studies the present authors studied aluminum oxidation by atmospheric-pressure dielectric-barrier discharges in diluted mixtures of oxygen with argon or nitrogen, utilizing a reactor with a gradient of temperature along the gas flow direction and a gradient of O_2 fraction, x_{O_2}, across. Substantial additional growth on 3-nm

thick native oxide layers on aluminum could be achieved, e.g. up to 10 nm within 3×10^3 s at 573 K. Even at room temperature an additional oxide thickness of 2 nm was reached within 300 s. The original focus of the present study was on the question what the role of the direct plasma exposure for these findings is, beyond the generation of strong neutral oxidants such as O atoms, singlet oxygen, and ozone. To this end the oxidation of sputtered aluminum films on silicon substrates exposed directly to the discharge and to the gas atmosphere in the pre-discharge (PrD) and the post-discharge (PoD) regions was studied, applying infrared absorption-reflexion spectroscopy (IRRAS) as a routine method for thickness measurement, calibrated by XPS on a smaller number of reference samples. Results of thickness measurements were compared with oxygen atom densities calculated by a simplified kinetic model.

Experimental Section

Materials

Silicon wafers (4 in diameter, 500 µm thickness, 10 to 20 Ωcm resistivity) were obtained from *MicroChemicals GmbH* (Ulm, Germany), borosilicate glass (Borofloat®) from *Schott AG*, Germany, 99.999% pure aluminum sheet (0.5 mm) from *Goodfellow* (Hamburg, Germany). Sodium salicylate, 99%, was purchased from *Thermo Scientific Chemicals* (Kandel, Germany). Process gases were mixed from argon (purity 6.0) and oxygen (6.0) or from argon and an Ar-O_2 mixture with 100 ppm O_2 (*Linde AG*, Germany).

Instrumentation and Experimental Parameters

Sputter Deposition of Al Films

Aluminum films with thicknesses between 90 and 120 nm were DC sputtered onto Si wafers using an industrial in-line coating system with load lock and three process chambers, equipped with a planar Al target (12.7 cm × 25.4 cm, purity 99.999%), powered with 1 kW. The base pressure was below 1×10^{-4} Pa. Ar (5.0) was used as process gas, with a gas flow of 200 cm³/min STP. The operating pressure was maintained at 1 Pa using a butterfly valve. After Al deposition the wafers were cut into samples of 1 cm × 2 cm size.

DBD-Based Plasma Oxidation

Experiments reported in this paper were performed at ambient pressure using a parallel-plate DBD setup with an asymmetric electrode arrangement consisting of a 1-cm thick grounded aluminum base plate and a 0.2-cm thick borosilicate glass dielectric. The high-voltage electrode was glued onto a 0.07-cm thick borosilicate-glass carrier sheet mounted on top of the 0.2-cm thick dielectric, as shown schematically in Fig. 1. The basic construction is a flat flow channel with inner dimensions of 18 cm in length and 2.05 cm in width, to accommodate gapless rows of 2-cm wide samples with a length of 1 cm in gas-flow direction (*y* coordinate). An open height of 0.25 cm of the empty DBD reactor is defined by 2-cm wide, 0.25-cm thick borosilicate glass strips as side walls, placed between the Al base plate and the glass top plate. With 500-µm thick samples, the resulting gas gap width *h* is 0.2 cm. Up to 14 samples were placed in the reactor, generally starting with
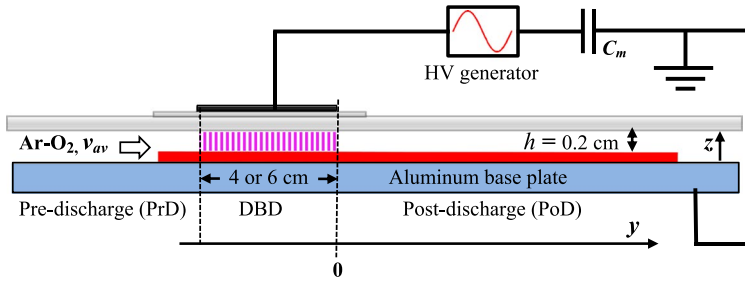
Fig. 1 Scheme (not to scale) of the DBD reactor with an aluminum base plate as ground electrode and borosilicate dielectric as top boundary of the flow channel. Gapless rows (red bar) of up to 14 samples (0.05 cm thickness $\times$ 1 cm in y direction $\times$ 2 cm across) were placed on the bottom of the reactor channel with an empty height of 0.25 cm, resulting in a 0.2-cm gas gap width h. y is zero at the transition DBD/PoD (Color figure online)

Table 1 Parameters used for oxidation experiments # 1 to 5

Parameters/#	1	2	3	4	5
x_{O_2}/ppm; x_{Xe}/%	20; 0	20; 1	100; 0	500; 0	500; 0
t/min	5–80	5–80	5–160	10–160	40; 60 (2:1 ms)
$U_{a,0}$/kV	3.4 ± 0.2	4.92 ± 0.08	3.57 ± 0.02	3.57 ± 0.01	3.60 ± 0.02
p_V/Wcm^{-3}	1.2 ± 0.2	1.29 ± 0.03	1.18 ± 0.08	1.23 ± 0.02	1.20 ± 0.03

one or two samples in the pre-discharge (PrD) region, four or six in the DBD region with length $L = 4$ cm or 6 cm, and up to nine in the post-discharge (PoD). In order to provide an undisturbed laminar gas flow along the row of samples, dummy samples (not shown in Fig. 1) were used to fill the 5-cm long pre-discharge region to avoid a step in gap width. The average gas flow velocity v_{av} was 150 cm/s in all experiments, resulting in average residence times of 27 and 40 ms with $L = 4$ and 6 cm, respectively. The high-voltage generator (model *7020 UZ* from *SOFTAL electronics GmbH*, Hamburg, Germany) is connected to a rectangular metal foil or metal mesh electrode glued to the top of the thin glass carrier sheet.

The sinusoidal voltage applied to the discharge arrangement $U_a(t)$ as well as the transferred charge $q(t)$ were measured using a high-voltage probe (*Tektronix P6015A*) and a series capacitor C_m (560 pF), respectively. An oscilloscope (*LeCroy WR604Zi*) was used to monitor $U_a(t)$ and the voltage drop $U_C(t)$ at the capacitor to calculate the dissipated power P. The measured frequency was 16.1 kHz. O_2 fractions x_{O_2} and, in series 2, the Xe fraction x_{Xe}, oxidation durations t, voltage amplitudes $U_{a,0}$ and power densities $p_V \equiv P/V$, (plasma volume $V = 1.64$ cm^3 at $L = 4$ cm or 2.46 cm^3 at $L = 6$ cm) dissipated during the experiments are given in Table 1. In one experiment in series 5 the excitation was pulsed, with $t_{pulse} = 2$ ms and $t_{pause} = 1$ ms. The primary voltage settings at the HV generator were adjusted to obtain about the same power densities for all oxidation runs.

Gas flow controllers were from *MKS Instruments Deutschland GmbH* (München, Germany). The oxygen concentration in the gas was checked repeatedly before and after the DBD operation, using a Portable O_2 Analyser BA 4510 (*Bühler Technologies GmbH*, Ratingen, Germany).

After IRRAS measurements to determine the oxide thickness at zero oxidation time, the samples were placed inside the reactor, oxidized for n min ($n = 1$, 5, or 20), measured again, oxidized for another n min, measured, oxidized $2 \times n$ min and so on, up to the maximum total oxidation duration. We assume that the effects of an intermediate sample exposure to the atmosphere such as hydratization and contamination is remedied during the following oxidation within a time which is negligible compared with the shortest treatment interval.

XPS Measurements on Aluminum Oxide Films

On selected samples, oxide thickness or stoichiometry were measured by X-ray photoelectron spectroscopy (XPS), using a *PHI 5500 ESCA* system (*Physical Electronics*) equipped with a hemispherical analyzer and a Mg Kα X-ray source (1253.6 eV). The angle between X-ray source and analyzer was 54.7°. High-resolution spectra were acquired at a constant analyzer pass energy of 11.75 eV and an electron take-off angle of 47° with respect to the sample surface. The *PHI MultiPak* instrument software was used to evaluate the spectra.

To measure the oxide thickness, Al 2p core-level spectra were acquired and curve-fitted to determine relative peak areas (intensities) of metallic and oxidic peaks, I_m and I_o, respectively. Fitting parameters defining the asymmetry of the metallic peak were obtained from the spectrum of an argon sputter-cleaned sample of pure aluminum. The oxide thickness X was calculated according to Strohmeier [28] and Alexander [29], using Eq. (1):

$$X = \lambda_0 \sin(\theta) \ln\left(\frac{N_m \lambda_m I_o}{N_o \lambda_o I_m} + 1\right) \tag{1}$$

where "m" and "o" indicate metal and oxide, respectively. $N_{\{m,o\}}$ are number densities of aluminum atoms, $\lambda_{\{m,o\}}$ effective attenuation lengths of photoelectrons. Both quantities were calculated with mass densities $\rho_m = 2.7$ g/cm^3 for Al and $\rho_o = 3.1$ g/cm^3 for the oxide. θ is the electron take-off angle with respect to the sample surface.

Effective attenuation lengths $\lambda_{\{m,o\}}$ were calculated from inelastic mean free paths (IMFP) and transport mean free paths (TMFP), following Jablonski and Powell ([30], eqs. (7), (18) and (20)]. For metallic Al, IMFP and TMFP values were interpolated from data in refs. [30, 31]. For the oxide, IMFP was calculated using the TPP-2 M formula from ref. [32], and TMFP according to ref. [30], using transport cross-section data from *NIST Electron Elastic-Scattering Cross-Section Database* [33]. Results are $\lambda_m = 2.22$ nm and $\lambda_o = 2.94$ nm.

Since Al(III) oxides and hydroxides cannot be distinguished by the Al 2p binding energy, the oxidic peak component represents both oxide and hydroxide states, which may result in an underestimation of the calculated overlayer thickness [29].

FT-IRRAS Measurements of Oxide Thickness

As a routine method to determine X before and after oxidation runs, FTIR measurements were performed in the infrared-reflexion absorption (IRRAS) mode, using a Nicolet iS50 spectrometer (*Thermo Fisher Scientific GmbH*, Dreieich, Germany). The instrument was equipped with an MCT/A detector and a Smart SAGA reflexion accessory with an integrated polarizer to remove s-polarized light, and an oval 1.6 cm × 0.8 cm aperture. Average angle of incidence and spectral resolution were 80° and 4 cm^{-1}, respectively. For the background spectrum, a gold mirror was used (Au-coated glass). 256 scans and 64 scans were

averaged for background and sample measurements, respectively. The wavenumber-integrated absorbance of the LO mode absorption of Al_2O_3 with a maximum near 950 cm^{-1} [34] was obtained using the integration facility of the *OMNIC* software package (*Thermo Fisher Scientific*). Therefore, wavenumber limits of 1050 and 750 cm^{-1} were applied. The former limit was chosen relatively narrow in order to avoid possible contributions from any adsorbates. The integrated absorbance is proportional to the aluminum oxide thickness [35]. In order to calibrate the IRRAS data, thickness measurements were performed by XPS on 15 samples with $3.5 \leq X/nm \leq 7.0$. Linear regression resulted in relation Eq. (2) between X and integrated absorbance $A_{750\text{-}1050}$.

$$X/\,nm = 2.63 \pm 0.06 \,\times\, A_{750-1050}/cm^{-1} \tag{2}$$

Measurements of Relative Radiant Flux Density on the Sample Surface

To obtain the distribution of radiant flux density of VUV photons on the sample surface PrD and PoD regions adjacent to the DBD as a function of distance D from the discharge edge, scintillator dots from slightly compressed sodium salicylate [36] powder were used, as shown schematically in Fig. 2. For these measurements, the open reactor channel height was enlarged to 4 mm in order to arrive at $h = 0.2$ cm, as in the oxidation experiments, with an inserted 2-mm thick polished Al sheet. The salicylate powder was pressed into 0.5-mm deep blind holes of 3 mm diameter drilled into the sheet, arranged in a row as schematically shown in Fig. 2. The lateral displacement of consecutive dots prevents any disturbance of the light path from the discharge arriving at a selected spot. It is important that the surface of the pressed powder is exactly on the same level as the surrounding metal surface. An Ocean Optics spectrometer QE65000 and a lightguide P400-2-SR with collimator, all from *Ocean Insight* (Duiven, The Netherlands), were used to measure the fluorescence emission. For measurements in the discharge, a metal mesh was used as top electrode; the measured emission was corrected for the mesh's optical transmission.

In addition to measurements with variation of D (see Fig. 2) at 100 ppm O_2, the dependence on the oxygen fraction was also investigated, using a dot at $D = 1$ cm. To slow down degradation of the salicylate by photolysis and oxidation by O atoms, measurements were done with pulsed plasma excitation (1-ms pulses, 10-ms pauses) in the pre-discharge region upstream from the DBD. Results of these measurements are shown below in Figs. 5 and 6.
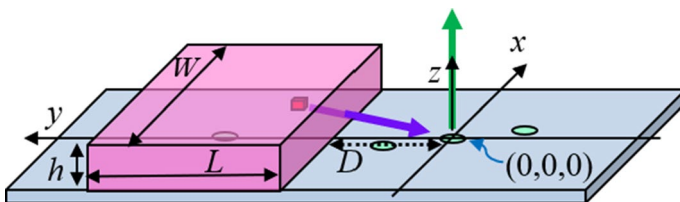

Fig. 2 Principle of measurements of the relative radiant flux density of VUV photons on the sample surface, here represented by a 2-mm thick polished aluminum sheet (blue), carrying a row of blind holes (diameter 3 mm, depth 0.5 mm) filled with slightly compressed sodium salicylate powder (green). These scintillator dots are irradiated (violet) from volume elements in the discharge (red), vertically emitted fluorescence light (green) is collimated and guided to a spectrometer. The shown coordinate system is used in Eq. (3) (Color figure online)

Fig. 3 Number density profiles of oxygen atoms in an Ar-O$_2$ mixtures flowing through a DBD (pink) and the adjacent PoD zone: Molar fractions of O$_2$ in the inflowing gas x_{O_2}/ppm are indicated at the curves. For other parameters see the inset legend (Color figure online)
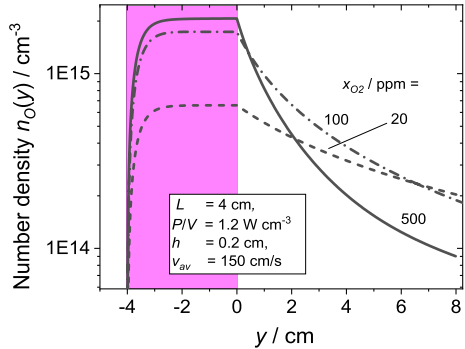
Software for Evaluation of Experiments and Numerical Calculations

OMNIC (version 7.2) and *Phi MultiPak* instrument software packages were applied to collect and evaluate FTIR and XPS spectra, respectively. *SpectraRay/4* from SENTECH *Instruments GmbH* (Berlin) was used for optical calculations, *OriginPro 2019* for curve fitting and data plotting. Numerical solutions of differential equations were obtained using the CVODE method option of the freely available *WinPP* software[1] with typically 1,000 time steps. Software from *COMSOL Multiphysics GmbH* (Göttingen) was used for CFD calculations.

Results

Model Results: Spatial Profiles of Oxygen Atoms

In Fig. 3 number density profiles of oxygen atoms are shown as a function of the spatial variable, y, specifying the location in the reactor. At the exit of the DBD zone y is chosen to be zero (as shown in Fig. 1). The species densities were calculated by a plug-flow model described in detail in a recent paper [37], based on the assumption that the discharge is a uniform source of long-lived excited argon species, collectively called Ar*. The set of Ar* species includes atoms in one of the four Ar($1s_i$) states, with $2 \leq i \leq 5$, as well as triplet argon excimers, Ar$_2$*. Oxidation experiments as well as calculations for the curves shown in Fig. 3 were run with O$_2$ starting fractions as low as 20, 100, and 500 ppm, in order to achieve a high degree of dissociation and a low recombination rate in the post-discharge, i.e., a large usable length downstream from the discharge where samples can be placed. In ref. [37] the validity of model calculations was checked by optical emission spectroscopy, resulting in an agreement within 10% for a double-dielectric channel with a 0.14 cm gap and for an asymmetrical channel with Al base plate and $h = 0.25$ cm, while larger discrepancies were observed for narrower channels with $h = 0.075$ cm and 0.11 cm for the double-dielectric and the asymmetric arrangement.

As a function of the input oxygen fraction x_{O_2}, the O-atom density at the DBD exit, $n_O(0)$, is at maximum $(2.1 \times 10^{15}$ cm$^{-3})$ at 400 ppm, under the conditions used here. Beyond this

---

[1] http://www.math.pitt.edu/bard/xpp/xpp.html

oxygen fraction, recombination reactions decrease the maximum number density of O atoms to be achieved. Therefore, increasing x_{O_2} by a factor of five from 20 to 100 ppm still increases $n_O(0)$ by a factor of three while there is only a small further increase of $n_O(0)$ at $x_{O_2} = 500$ ppm. It is important to note that eventually, at $y > 5$ cm, a situation is achieved where $n_O(y)$ is nearly the same in the x_{O_2} range from 20 to 100 ppm.

Increasing the electrode length from 4 to 6 cm and therefore the residence time from 27 to 40 ms, all other parameters being equal, leaves $n_O(0)$ virtually unchanged. Pulsing the 6-cm discharge with 2-ms pulses and 1-ms pauses (duty cycle ratio $= 0.66$) decreases $n_O(0)$ by a factor of 0.76, from 2.1 to 1.6×10^{15} cm^{-3}.

Radiant Flux Density of VUV Photons on the Sample Surface

Figures 4 and 5 show the results of VUV irradiance measurements for varying distance from the discharge edge D and varying fraction of O_2, x_{O_2}, respectively.

Fig. 4 Decay of VUV irradiance of the aluminum surface Φ with growing distance D from the DBD edge, normalized by dividing through the irradiance in the discharge zone at $D = -1$ cm (red). The blue curve is the normalized irradiance, calculated without reflected contributions by Eq. (3) (Color figure online)
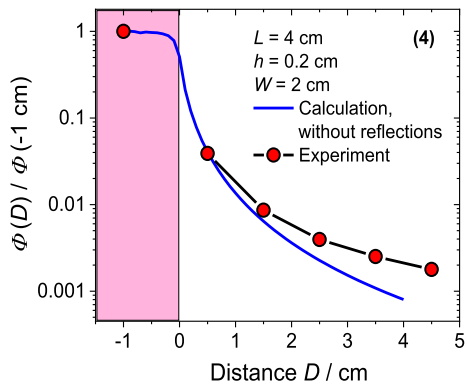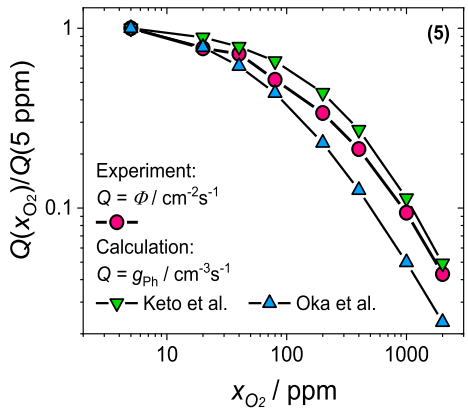

Fig. 5 Quenching of the VUV irradiance by O_2 (red). Model results (blue and green triangles) were obtained by model calculations using different published values of the rate coefficient for energy transfer from Ar excimers to O_2: 26×10^{-11} cm^3 s^{-1} (blue, from Oka et al. [42]) or 4.6×10^{-11} cm^3 s^{-1} (green, from Keto et al. [43]) (Color figure online)

For a point on the sample surface at distance D from the DBD edge the D-dependence of direct VUV irradiance can be written using the definition of an "energy efficiency" of VUV-photon generation η (see Fig. 2):

$$\Phi(D) = \frac{P\eta}{4\pi E_{ph} \, W \, L \, h} \int_{-W/2}^{W/2} \int_{D}^{D+L} \int_{0}^{h} z\left(x^2 + y^2 + z^2\right)^{-1.5} \mathrm{d}z \cdot \mathrm{d}y \cdot \mathrm{d}x \qquad (3)$$

The integrand represents the ratio $\cos(\alpha)/r^2$, where α is the angle between the light beam and the z axis, r the distance of an emitting volume element from the position $(0,0,0)$. The graph of the relative irradiance, obtained by dividing through the irradiance of a point in the DBD at $D = -1$ cm, is shown as a blue curve in Fig. 4. Up to $D = 1.5$ cm the fraction of direct light rays falls to about 70% of the total VUV irradiance which is 0.9% of the reference value in the DBD. With a power density of $p_V \equiv P/(W \times L \times h) = 1.2$ W/cm^3 (Table 1), taking $\eta = 0.1$ as a typical value of the fraction of discharge power which can be converted to VUV radiation, and photon energy $E_{ph} = 9.8$ eV for the argon excimer [38], the reference quantity $\Phi(-1 \text{ cm})$ amounts to an irradiance of 6.8×10^{15} cm^{-2} s^{-1}, which is close to the calculated value of $p_V \eta h/(2E_{ph}) = 7.7 \times 10^{15}$ cm^{-2} s^{-1} for a DBD with infinite extension.

The effect of quenching by O$_2$ is shown in Fig. 5, using argon with a virtually negligible addition of 5 ppm O$_2$ for the reference measurement. The observed dependence on x_{O_2} is in reasonable agreement with calculations of the generation rate of VUV photons g_{Ph} by radiation from Ar atoms in resonant state and from Ar excimers, based on a zero-dimensional steady-state model as in ref. [39]. This model uses excitation coefficients of Ar(1s) states and bimolecular quenching rate coefficients for their reactions with O$_2$ from refs. [40, 41]. The corresponding rate coefficients for Ar excimers were taken from Oka et al. [42] (26×10^{-11} cm^3 s^{-1}), or from Keto et al. [43] (4.6×10^{-11} cm^3 s^{-1}), resulting in the data points marked by blue and green triangles.

Plasma Oxidation Results

Figure 6 shows raw data from the oxidation experiments: oxide thicknesses X at different positions y in the reactor, after the indicated total oxidation time t, obtained in the series 1 to 4 specified in Table 1, with starting oxygen fractions of 20, 100, and 500 ppm, respectively.

As Fig. 6 reveals, the native oxide on the samples, which were prepared several months before they being used in these experiments, has grown to between 3.1 and 3.6 nm. These values are in reasonable agreement with data reported by Hass [9] as well as more recently by Evertsson et al. [10], see above, and are close to the "limiting thickness" under ambient conditions, in the sense of the original CM theory. Nevertheless the oxidation rate achieved in most of the here-reported experiments at the lowest oxidation duration of 5 min was generally sufficient to obtain a thickness $X(5 \text{ min})$ which was virtually the same as if the oxidation had started with $X(0) = 0$ nm, due to the characteristic time-dependence of $X(t)$ according to CM theory (see below). Exceptions are seen if $X(0)$ is relatively large and the oxide growth slow, see, e.g., the 100-ppm results in Fig. 8, yellow curve and data points.

In the presence of atomic oxygen in the DBD as well as the post-discharge, the oxide thickness rapidly grows beyond the starting value: In all cases a substantial increase of X is observed in the DBD region, indicated by the pink rectangle, but also in the
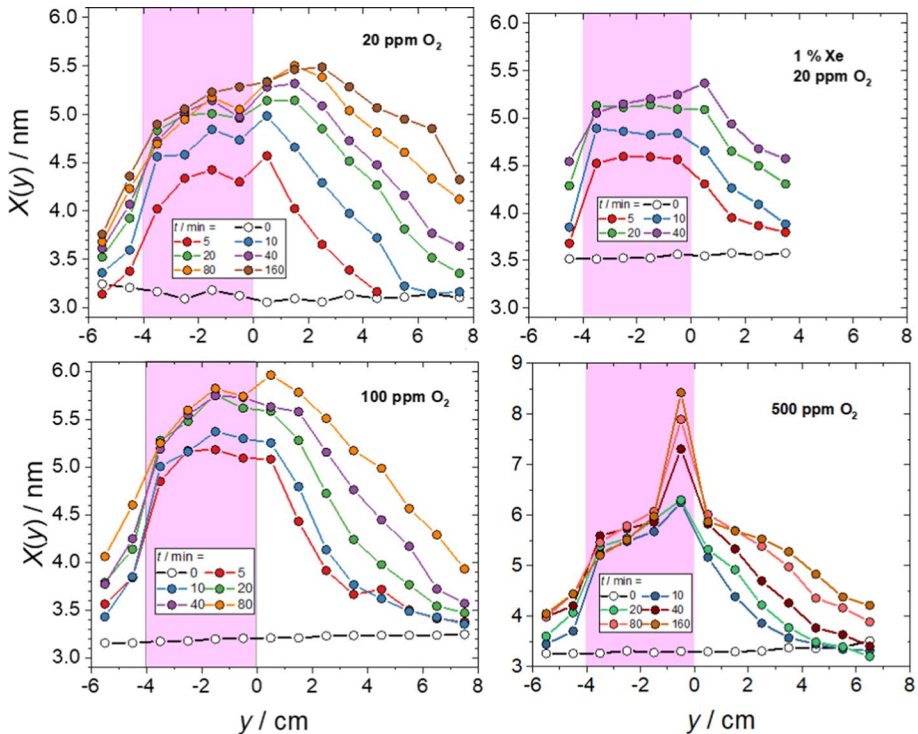
Fig. 6 Oxide thicknesses as measured by IRRAS after exposure to the gas atmosphere in front of the DBD (pre-discharge, PrD), in the DBD (pink), and in the post-discharge (PoD) zone up to a distance of 7.5 cm from the DBD in case of the series with 20 and 100 ppm O_2, respectively. In general, exposure durations of individual runs were increased logarithmically; the total durations are indicated in the legend. Note that significant oxidation always takes place also in the pre-discharge zone, up to at least 1.5 cm upstream from the DBD. In order to facilitate the comparison of results, the same ranges of y and X were used, except for the graph with results of the 500-ppm experiment (Color figure online)

post-discharge (PoD), at least up to the maximum studied distance. Interestingly, significant oxide growth also takes place in the region upstream from the discharge (pre-discharge, PrD). Samples were placed here to investigate if the excimer radiation emitted from the discharges onto their surfaces would result in additional oxide growth. The possibility, that the growth rates observed upstream from the discharge are due to a diffusion of reactive species, O or O_3, from the discharge against the gas flow can be excluded, see below.

The motivation to use O_2 fractions as low as 20 ppm was the attempt to achieve a high degree of dissociation, small density of recombination products O_3 and $O_2(a)$, and an extended post-discharge (PoD) region with substantial oxygen-atom densities. The results shown in Fig. 6 in fact demonstrate that significant oxidation can still be measured at a distance of 7.5 cm from the trailing edge of the discharge zone. Surprisingly, however, the oxidation rate in the PoD with 20 ppm O_2 in Ar is larger than to be expected from the rates achieved in the DBD, based on the premise that atomic oxygen is the main oxidizing species in the DBD and the PoD: In the experiment a strong overshoot in $X(y)$ is noted at $y < 3$ cm and extrapolating the nearly linear portions of the $X(y)$ relation with negative

slope in the PoD back to $y=0$ results in a thickness which is up to about 0.5 nm larger than the average of X values achieved in the DBD, at $y=-2.5, -1.5$, and -0.5 cm. Note that for $t>20$ min, there is even an initial increase of X in the PoD, at variance from the behavior of $n_O(y)$ in Fig. 2.

A further surprising result of this series is that the oxidation eventually virtually stops at an oxide thickness of about 5.0 nm within the DBD and of 5.3 nm at around $y=1$ cm in the PoD. This observation is in contrast to what is expected, based on CM theory, from the oxide growth at $t<40$ min. At larger distance from the discharge, at around 5 to 7 cm from the DBD, on the other hand, the oxidation process appears to continue up to the largest time studied, 160 min.

In order to investigate if this behavior is related to vacuum ultraviolet (VUV) irradiation of the sample surfaces in and close to the DBD, due to the optical emission from Ar_2^* excimers at 126 nm, an experiment was run with 1% xenon added to the gas mixture, with a reduced number of samples. In this gas mixture, long-lived Ar* species are efficiently deactivated by collisional energy transfer to Xe atoms, resulting in a shift of the main optical emission from around 126 nm to a broad continuum centered at 172 nm, due to Xe_2^* excimers [44]. In fact, the overshoot of X in the early PoD region is largely removed by the Xe addition while the $X(3.5$ cm$)$ values are similar with and without Xe.

The addition of larger amounts of oxygen also largely removes the overshoot of X in the early PoD: With 100 ppm O_2, $X(0.5$ cm$)$ is generally smaller than the oxide thickness achieved at $y=-0.5$ cm in the DBD. With 500 ppm O_2 in the mixture, a qualitative change of the process is observed: According to the model calculations, the O-atom concentration in the DBD is hardly different from the case with 100 ppm O_2, the density of long-lived Ar species and, in parallel, the emission of VUV radiation at 126 nm is reduced further as Fig. 5 shows. Owing to the faster reactions of O atoms with O, O_2 and O_3, oxidation rates in the PoD at intermediate times, e.g. 40 min, are substantially smaller at 500 ppm than with 100 ppm O_2. Most prominent, however, is the significantly increased oxide thickness, up to 8.4 nm, on the "last" sample in the DBD zone, i.e., the sample located closest to the DBD exit, and the virtual absence of a limiting thickness.

In order to determine the cause for the phenomenon of a locally strongly increased oxidation rate, further experiments were run with 40-min oxidation time, employing a 4-cm foil electrode and, to enable optical access to the discharge, a 4-cm mesh electrode, as well as with a 6-cm mesh electrode. With the latter, the normally applied CW excitation was used as well as pulsed excitation, with pulse and pause durations of $t_{pulse}=2$ ms

Fig. 7 Results of experiments with oxidation times of 40 and 60 min, respectively, employing 4- and 6-cm discharge zone lengths, respectively. Effect of pulsed plasma excitation
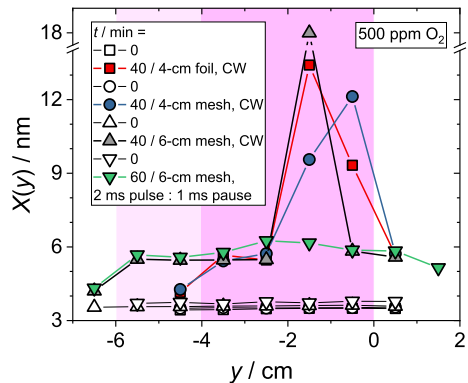
and $t_{pause} = 1$ ms, respectively, and $t = 60$ min in order to keep the total on-time at 40 min Fig. 7. The latter experiments were guided by the conjecture that a negatively charged species, trapped in the gas gap and accumulating near the downstream end of the discharge, could possibly be responsible for the accelerated oxidation. One important result of these runs was that the location of the oxidation rate maximum does not depend on the residence time of the gas as one would it expect for the major neutral species involved, but on the distance to the trailing edge of the discharge. Even more significant, pulsing the discharge with a 3-ms period, i.e., about 13 cycles during the passage of the gas through the 6-cm long DBD zone, largely removed the inhomogeneity in $X(y)$ (see the green data points).

Surface Morphology of Oxidized Samples

In spite of the filamentary character of DBDs used in the present study, the sample surfaces generally do not exhibit craters, nanoparticles or any other non-uniformities due to prolonged exposure to the discharges. Figure 8 shows two scanning electron micrographs

Fig. 8 Scanning electron micrographs of sample surfaces after oxidation. Top: Al/Si, field size: 110 μm × 75 μm. Bottom: Al sheet, 1100 nm × 750 nm
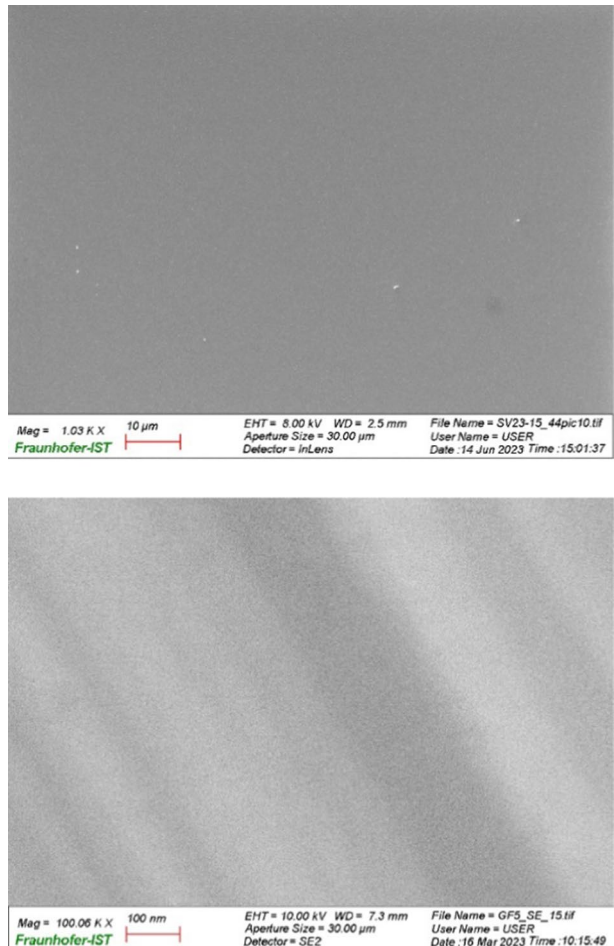
taken from samples exposed for 160 min to DBDs in Ar with 500 ppm admixed O_2. For the bottom micrograph a manually polished Al sheet was oxidized instead of otherwise used sputtered Al films in order to avoid the nanogranular surface topography typical for sputtered metals. The micrograph shows only fine striae from polishing.

Evaluation and Discussion of Experimental Results

Evaluation of Raw Data in Terms of Cabrera–Mott Theory

The experimental data are interpreted in terms of the Cabrera–Mott theory of low-temperature metal oxidation [13] where the differential growth Eq. (4) plays a central role. Parameters X_1 and u of this equation are defined in Eqs. (5) and (6):

$$\frac{dX}{dt} = 2\,u\,\sinh\left(\frac{X_1}{X}\right) \tag{4}$$

$$u = \Omega\,n\,\nu\,\exp\left(\frac{-W}{k_B T}\right) \tag{5}$$

$$X_1 = -\frac{q\,a\,V_{CM}}{k_B T} \tag{6}$$

In Eq. (5), Ω is the volume of oxide per metal ion, 0.0233 nm^3, $n = 10$ nm^{-2} the maximum number of Al atoms per unit area at the metal/oxide interface which can "jump" over the rate-limiting energy barrier W on the potential energy curve to become an Al_3^+ ion in the first interstitial position in Al_2O_3, seen from the metal. ν is the attempt frequency of the jump ($\approx 10^{12}$ s^{-1}), $\nu\exp(-W/k_B T)$ the rate at which the jump actually takes place in the absence of an electric field. In Eq. (6), q is the charge of the migrating cation (in amorphous Al_2O_3, with Al^{3+} as the migrating ion, 3 elementary charges, $e = 1.602 \times 10^{-19}$ C), $a = 0.11$ nm is half the distance of two neighboring potential minima for interstitial cations in the oxide, V_{CM} the Cabrera–Mott potential and k_B the Boltzmann constant. (Numerical values are taken from refs. [8, 15].) For ultrathin oxide films at room temperature $2\sinh(X_1/X) \simeq \exp(X_1/X)$. The effect of this factor is to reduce the energy barrier from W to $W + q\,a\,V_{CM}/X$ (note that $V_{CM} < 0$) and thereby increasing the jump rate of Al atoms. $|V_{CM}|/X$ is the absolute value of electric field strength across the oxide film.

Equation (4) cannot be solved in a closed form. The authors themselves presented an approximate solution for $X(t)$, based on the concept of a "limiting thickness" X_L, arbitrarily defined as the thickness at which $dX(t)/dt$ has decreased to below 10^{-13} cm/s, i.e., below about 0.1 nm per day. The "inverse-logarithmic" oxide-growth law is given by Eq. (7), with parameters A and B depending on u, X_1, and X_L.

$$\frac{1}{X} = A - B\,\ln(t) \tag{7}$$

A different approximate solution was published by Ghez [45], enabling, in principle, a direct determination of u and X_1 from a suitable plot of experimental data. However, our attempts to use Ghez' equation to retrieve these parameters from synthetic $X(t)$ functions,

generated by numerical integration of Eq. (4), failed for relatively small values of X_1. The approximative nature of Ghez' solution was already noted by others [46].

Therefore, we used a different approach, based on nonlinear implicit fitting of experimental data to Eq. (4). To obtain the required expression for the time derivative of X as a function of t with a limited amount of experimental data, we used Eq. (7) as an empirical equation to determine A and B by linear regression and to gain an empirical equation for the oxide thickness $X(t)$. Thereof $dX(t)/dt$ was calculated and equated to the right-hand side of Eq. (4):

$$\frac{B}{[A - B\ \ln(t)]^2\ t} = 2\ u\ \sinh\left(\frac{X_1}{X}\right) \tag{8}$$

In this manner we arrive at a transcendental equation allowing to extract the basic parameters of CM theory, X_1 and u, from a nonlinear implicit fit to the experimental data $X_i(t_i)$, using A and B as constants. This approach avoids both, using the CM concept of a limiting thickness X_L as well as the application of Ghez' equation, and it directly yields X_1 and u.

Presentation and Discussion of X(t) Data

The Nomenclature, Data Points Excluded from CM Evaluation

Figure 9 shows the results of applying the evaluation method outlined in the previous section to the experimental data. Bent continuous lines are graphs of numerical solutions of Eq. (4) with the parameters u, X_1 shown in the figure legends.

Names like, for example, "PrD0.5" or "PoD3" are used to denote data representing the pre-discharge region at 0.5 cm from the leading edge of the DBD or the post-discharge zone at 3 cm from the trailing edge of the DBD. Occasionally prefixed numbers like in "100PoD5" are values of x_{O_2}. Data pairs measured in the PoD at, e.g., $y = 0.5$ and 1.5 cm or at 2.5 and 3.5 cm were averaged to give $X(1\text{ cm})$ and $X(3\text{ cm})$, respectively. To represent oxide thickness in the DBD, values of X measured at $y = -2.5, -1.5$, and -0.5 cm were averaged, with the exception of data obtained with 500 ppm O_2, where "DBD1" and "DBD2" are $X(-2.5)$ and $X(-0.5)$, respectively.

There are two kinds of systematic deviations from CM behavior where experimental data points were justifiably excluded from the fitting procedures: (1) Failure of the assumption that the finite starting oxide thickness at $t = 0$ between 3.1 and 3.6 nm can be neglected for the lowest oxidation times of 5 or 10 min and (2) significant lagging behind of the oxide growth, relative to an extrapolation, based on CM theory, of the behavior at earlier times. In Fig. 9, single data points excluded from the CM fits are marked by an arrow symbol ending with a cross, multiple excluded data points are connected by a dot-dashed line to the last included point. The $X(5\text{ min})$ value was excluded only twice from the fitting procedure: in the evaluation of PoD3 with 1% Xe and 20 ppm O_2 and of PoD5 with 100 ppm O_2. In the latter case, data measured 7 cm from the DBD could not be fitted, but taking X_1 and u from the 20-ppm experiment to draw a $X(t)$ curve shows that the oxidation at $t > 20$ min does not proceed significantly different for 20 and 100 ppm O_2, respectively. Much more frequently, multiple or single data points had to be excluded at larger values of t, due to a significant retardation or even virtual stopping of oxide growth in the DBD or in the PoD at distances from the discharge up to 3 cm. Note that, in principle, at least three data points
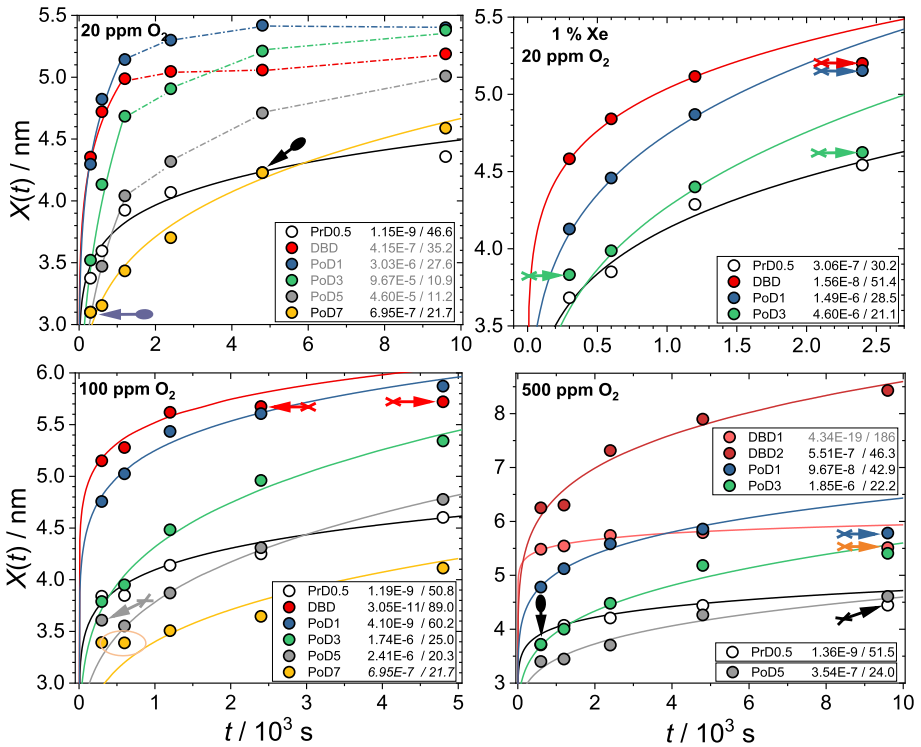
Fig. 9 Oxide thicknesses $X(t)$ at different positions in the DBD reactor, evaluated from the data shown in Fig. 4. Data denoted by "DBD" and, e.g., "PoD3" are averages of X at $y = -2.5, -1.5$, and -0.5 cm, and at $y = 2.5$ and 3.5 cm, respectively. Exception: Data named "DBD1" and "DBD2" are $X(-2.5)$ and $X(-0.5)$, respectively. Pairs of numbers like "2.41E-6/20.3" are the parameters u/nm×s^{-1} and X_1/nm, obtained as outlined in Sect. "Evaluation of Raw Data in Terms of Cabrera–Mott Theory" and used to calculate the graphs by numerically solving Eq. (4). Data points excluded from the evaluation are marked by arrows ending in crosses or by dot-dashed connecting lines. Arrow symbols ending in ovals are marking overlapped data points. Numbers given in grey are questionable, see discussion. Italic numbers for the case of 100 ppm O$_2$ were not fitted from the corresponding data but taken from the 20-ppm data

$X_i(t_i)$ are required to assess if the oxidation follows CM theory but two data points suffice to determine the parameters X_1 and u if a CM growth mechanism is postulated, as it was necessary for the curve PoD3 with 1% Xe and 20 ppm O$_2$.

In the following, the discussion will start with the oxidation induced by VUV photons in the pre-discharge zone and the effect of O atoms in the remote post-discharge region.

Effects of VUV Photons

As shown in Figs. 6 and 9, substantial oxidation takes place already in the pre-discharge (PrD) zone, up to a distance of 1.5 cm from the discharge edge. Interestingly the values of X_1 and u, determined at the location PrD0.5 for $x_{O_2} = 20$, 100, and 500 ppm O$_2$ in Ar fall into narrow ranges of 46.6 to 51.5 nm and 1.19×10^{-9} to 1.36×10^{-9} nm/s, respectively. (Data measured at PrD1.5 could not be evaluated by the fitting procedure.)

We attribute the oxidation in the pre-discharge to VUV photons emitted from the DBD. Acceleration of aluminum oxidation by irradiation of the metal with UV photons was

already reported in 1947 [47]: Within 8 days in dry air at room temperature the oxide layer grew to a thickness of 2.5 nm in the dark, but to 4.6 nm under illumination by a 4-eV photon flux of about 2×10^{16} cm^{-2}s^{-1} from a mercury-arc lamp, filtered through a 1-cm water layer to remove more energetic contributions which might result in generation of O atoms. Any potential involvement of photochemically produced ozone was also excluded by a control experiment with ozone-enriched atmosphere in the dark, where no oxidation enhancement was observed within several days. Cabrera explained the observed effect by an injection of electrons from the metal into acceptor levels of adsorbed oxygen species, resulting in an increased Cabrera–Mott potential [48]. According to his calculations the effect should have a very small dependence on photon flux but increase with the photon energy hν and possibly become "substantial" at energies of and beyond the oxide bandgap E_g. It is important to distinguish this physical effect from the chemical mechanism which is the basis of the oxidation by the UV/ozone (or "UVO") method in which the formation of O atoms is essential [49]. Cabrera's model was substantially extended by Chang and Ramanathan [50], including the concept of coupled ion and electron currents developed by Fromhold and Cook [51]. In these calculations, a strong acceleration of oxide growth and increase of X_L by 4-eV UV illumination was predicted. However, in following experimental studies no increased thickness by UV irradiation was found and the effect of photons was rather interpreted in terms of an improved oxide film quality, i.e., enhanced density and electrochemical impedance [52, 53]. Unfortunately, the applied photon flux and energy were not specified in these publications.

The experimental setup shown in Fig. 1 allows us to check Cabrera's expectation of substantially increased oxide growth rate at photon energies beyond the gap energy of Al$_2$O$_3$. The presence of O atoms or ozone in the pre-discharge region by diffusion from the DBD against the gas flow can be excluded at 150-cm/s gas velocity: Assuming constant gas velocity v across the reactor channel height h (plug flow), upstream diffusion of a species O$_n$ (O or O$_3$) produced in the discharge should result in a density profile proportional to exp$(-y' \times v/D_{On,Ar})$ where $D_{On,Ar}$ is the diffusion coefficient of O$_n$ in argon and y' the distance from the leading edge of the DBD. For O atoms, with $D_{O,Ar} = 0.38$ cm^2/s [54], the decay length $D_{O,Ar}/v$ at 150 cm/s (10 cm/s) is only 25 μm (380 μm $= 0.04$ cm). A simulation using COMSOL Multiphysics shows that the introduction of a parabolic profile does not change the situation significantly: Even with only $v = 10$ cm/s, the O density decays by more than an order of magnitude already over a distance of 0.1 cm [55]. Another potential explanation of oxidation upstream from the DBD, generation of O atoms by photo-dissociation of O$_2$ in the inflowing gas, can also be disregarded, due to the small average absorption coefficient of photons with energies in the 9.5 to 12 eV range. Between 100 and 130 nm, where Ar DBDs predominantly emit VUV radiation [56], O$_2$ has, with the exception of two narrow absorption lines at 120.5 and 124.4 nm, an absorption cross section below 1×10^{-18} cm^{-2} [57]: In an Ar-O$_2$ mixture with 100 ppm O$_2$ the absorption length is beyond 4 m. Therefore, the significant oxidation observed in the pre-discharge zone must be due to irradiation of the metal surface from the discharge. From results of the irradiance measurements presented above, photon flux densities of roughly 2×10^{14}, 1×10^{14}, and 0.5×10^{14} cm^{-2} s^{-1} are estimated at a surface point 0.5 cm from the edge of a DBD in Ar with O$_2$ fractions of 10, 100, and 500 ppm O$_2$, respectively. 1.5 cm from the DBD the irradiance is about 25% of these figures.

The energy of photons emitted by Ar excimers, 9.8 eV, surpasses the threshold energies of three different photophysical processes in irradiated Al/Al$_2$O$_3$ double layers which are of potential relevance for the oxidation process: (i) Internal photoemission (IPE) from the metal into the oxide film, into acceptor states of adsorbed oxygen species [48], or

through the oxide film into vacuum [58] at $h\nu > \chi_0$, where χ_0 is the height of the energy barrier between the Fermi level in Al and the bottom of the conduction band in Al_2O_3 ("metal/oxide work function"). Values of χ_0 between 0.7 and, more recently, 3.0 eV [59] have been reported in the literature. (ii) Generation of electron–hole pairs at $h\nu > E_g$. The optical band gap energy E_g is 8.8 eV in crystalline Al_2O_3 [60] but substantially lower in amorphous Al_2O_3, about 7 eV for the anodic oxide [58] and 6.7 eV for Al_2O_3 obtained by atomic-layer deposition, ALD [61]. (iii) Intrinsic photoemission of electrons from Al_2O_3 at $h\nu > (E_g + E_a)$, where E_a is the electron affinity of the oxide. In amorphous Al_2O_3, $E_a = 1$ eV so that this effect starts at $h\nu > 8$ eV.

The roles played by these processes for VUV-enhanced oxidation does not only depend on the photon energy but also on the film thickness X and the angle of incidence α: At 9.8 (7.2) eV photon energy, optical constants n and k of amorphous (evaporated) Al_2O_3 are 1.92 (2.02) and 0.70 (0.11), respectively [63]. Therefore, the oxide absorbs an appreciable amount of the impinging 9.8-eV radiation even at $X < 10$ nm, as shown in Fig. 10. At grazing incidence, a major part of the radiation is reflected, the reflected fraction increasing with the angle of incidence α, see Fig. 11.

For this reason, IPE of electrons from the metal into the oxide and into oxygen acceptor states, which is mainly responsible for VUV-enhanced oxidation, should eventually decrease with growing X, while the separation of photo-generated electron–hole pairs in the Cabrera–Mott field as well as photoemission from Al_2O_3 will gain relative importance. The latter two mechanisms are expected to impede oxidation, due to the generation of

Fig. 10 Fractions of incident photons absorbed in the metal A_{Met} and the oxide A_{Ox}, respectively, in Al/Al_2O_3 with X nm oxide thickness at $\alpha = 0°$
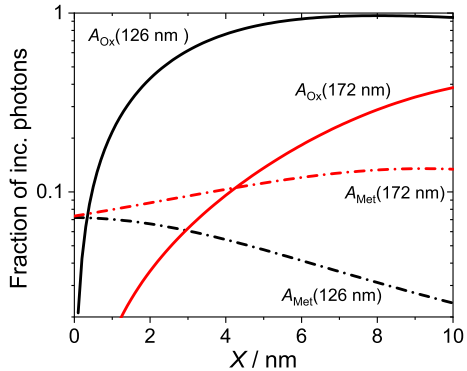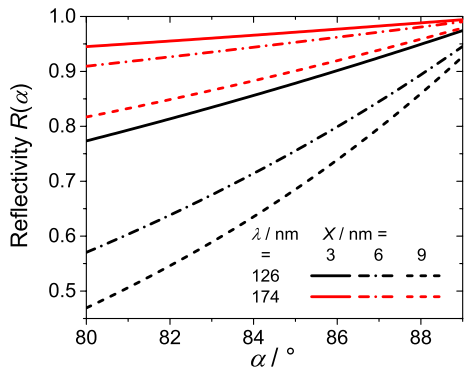

Fig. 11 Reflectivity under grazing incidence of Al/Al_2O_3 with X nm oxide thickness. Optical constants of Al and Al_2O_3 are taken from ref. [62, 63], respectively. (Calculation with *SpectraRay/4*)

positive space charges and/or polarization of the oxide, resulting in an electric field oriented against the CM field [64–66].

In the DBD zone the irradiance is at least an order of magnitude larger than at PrD0.5 or PoD0.5. Therefore, an impediment of oxide growth by the flux of photons beyond a certain thickness is a potential explanation for the surprising observation made with 20 ppm O_2 in Ar that the oxide thickness is larger in the near post-discharge region than in the DBD, see Fig. 6. With $x_{O_2} = 20$ ppm it was not possible to establish CM parameters X_1 and u, with the exception of PrD0.5 and PoD7 (Fig. 9); in all other cases the inverse log plots of data $1/X$ vs. $\ln(t)$ were convex towards the origin and could not reasonably fitted to a linear equation. So far it is an open question to what extent this is due to the VUV irradiance from the DBD, declining by nearly three orders of magnitude over the distance of 5 cm from the discharge.

In this context, the experiment with addition of 1% Xe is of interest, see Figs. 6 and 9. Here, deactivation of Ar(1s) species and Ar excimers by energy transfer to Xe results in a shift of the main emission band of the DBD from 9.8 eV to 7.2 eV [44]. The decreased photon energy results in lowered absorption in the oxide and enlarged absorption in the metal (Fig. 10). Therefore, the generation of electron–hole pairs should be substantially reduced. The so far limited experimental evidence of a reduced or even absent overshoot of oxide thickness in the close PoD (Fig. 6) is in agreement with the expectation that an impediment of oxidation is virtually absent.

In the follow-up to the present study, aluminum oxidation was studied in a special F-shaped reactor with two independent DBD sources of atomic oxygen and VUV radiation. In these experiments, which will be reported separately [67], it was seen that a reduction of the vertical VUV photon flux, as measured by the salicylate technique, by a factor of 0.65 reduced the film thickness achieved within 80 min, with the O-atom source switched off, by not more than 10 to 15%. $X(t)$ curves were virtually the same for $x_{O_2} = 20$, 200, and 2000 ppm, respectively, and followed the CM law (Eq. (4)) up to about 5,000 s, when a limiting thickness of 5.4 to 5.6 nm was reached. These results demonstrate the virtual independence on x_{O_2} and the small intensity dependence of oxidation enhanced by super-bandgap irradiation.

Oxidation by Atomic Oxygen

An exact independent establishment of CM parameters u and X_1 from $X_i(t_i)$ measurements requires a very small statistical error of experimental data; two different pairs u, X_1 can result in two functions $X(t)$ between which cannot be decided empirically, based on measurements made with a certain statistical error over a limited time interval. However, in the present study it appears reasonable to hypothesize that the variation of O-atom number densities in the remote PoD affects only the CM potential, i.e., X_1, but leaves the energy barrier height W and therewith u unchanged.

That is why an evaluation of results obtained 3 cm from the DBD and beyond was done with u fixed at 1.0×10^{-6} nm/s, which is about the average of the individual fitted values of u in Fig. 9 and corresponds to an energy barrier height W of 1.0 eV, if Ω, n, and ν are given the above-quoted values (see Eq. (5)). Interestingly, $W \approx 1$ eV can also be extrapolated from results of Reichel et al. [15] for room-temperature oxidation. Figure 12 shows the X_1 values obtained with this choice of a common parameter u. In general, the agreement is not significantly worse than in Fig. 9. Using Eq. (6) the obtained values of X_1 were converted to CM potentials V_{CM} which are related to the calculated number densities of atomic oxygen n_O, see Fig. 13. Converting O-atom number densities into partial pressures p_O and fitting a straight line to data points $-V_{CM}$, $\log(p_O/\text{Pa})$ results in the empirical

Fig. 12 CM evaluation of selected series using u fixed at 1.0×10^{-6} nm/s. Figures at curves are X_1 values. Note that 100PoD7 data could not be fitted (see above) but they are close to the green curve obtained with data of 20PoD7, as expected in view of the converging O-atom densities, see Fig. 3 (Color figure online)
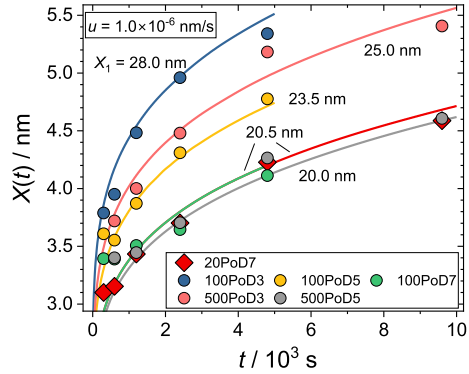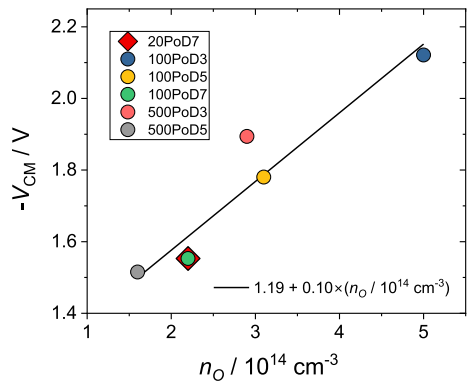

Fig. 13 Plot of V_{CM} as determined from X_1 values in Fig. 12, using Eq. (6), as a function of calculated oxygen-atom number densities n_O (Fig. 3)

equation $-V_{CM} = 1.68 + 1.35 \times \log(p_O / Pa)$ in the partial-pressure range of $0.67 < p_O / Pa < 2.08$. Theoretically, one should not expect a pre-logarithmic factor larger than $\ln(10) \times k_B T/(ze)$ when the chemisorption reaction of O or O_2 follows the scheme $O_n(gas) \rightarrow O_n(ps)$ and following $O_n(ps) + z \times e(metal) \rightarrow O_n^{z-}$ (cs) (ps = physisorbed, cs = chemisorbed, $n = 1$ or 2) [1, 68]. At room temperature this factor is 0.06 V and 0.03 V for $z = 1$ and 2, respectively. Experimentally, an increase of V_{CM} by 0.07 eV was actually reported for pressure jumps of pure O_2 from 1 to 10 and from 10 to 100 Pa, in good agreement with the expectation [1]. A much larger pre-logarithmic factor, on the other hand, 0.36, was reported [69], based on results by Cai et al. [11] for the O_2-pressure range from 10^{-6} to 10^{-3} Pa. A detailed discussion of the even larger factor established here is beyond the scope of this paper. For the moment it may suffice to point out that in the present experiments the gas phase contains, aside from O atoms, other oxygen species (O_2, O_3) with number densities beyond 10^{13} cm^{-3} (0.4 ppm) which may contribute to heterogeneous reactions involved in the oxidation process. For this reason, a reaction scheme as simple as given above might be far from the reality.

Oxidation in the DBD Zone

Without much more experimental work a well-founded discussion of $X(t)$ data measured in the DBD is rendered virtually impossible due to the combined effects of atomic oxygen and high fluxes of energetic photons. In general, a critical thickness X_C between 5 and

6 nm is reached within about 1,000 s, beyond which the oxidation process virtually stops or proceeds with a greatly reduced rate. The reason for this observation is probably the disappearance of sufficiently rapid electron transport from the metal through the highly insulating oxide to the oxygen acceptor at the oxide/gas interface [68].

In view of the limitation of oxide thickness to be achieved at room temperature by exposure to atomic oxygen as well as to the irradiance by VUV photons it is all the more surprising to find, with $x_{O_2} = 500$ ppm, that on the sample in the DBD at $y = -0.5$ cm ("DBD2" in Fig. 9) a thickness of 8.4 nm is achieved after 9,600 s, while at $y = -2.5$ cm ("DBD1" in Fig. 9) oxide growth virtually stops at a thickness of 5.6 ± 0.1 nm, achieved within 600 s. An alternative CM evaluation of the $X(-0.5,t)$ data with u fixed at $u = 1 \times 10^6$ nm/s results in $X_1 = 42.5$ nm, i.e. $V_{CM} = -3.22$ V. More detailed investigations into this phenomenon, comparing DBD zone lengths L of 4 and 6 cm, respectively, and pulsed excitation of the discharge, see Fig. 7 and the last paragraph of Sect. "Plasma Oxidation Results", lead us to postulate a qualitatively different oxidation mechanism to prevail in this case, in the downstream region of the DBD zone: The main findings, (i) oxide growth to nearly 20 nm within 9,800 s, virtually without a critical thickness X_C below 20 nm, (ii) downstream shift of the high-rate region and (iii) 50-% increase of the achieved thickness when L is enlarged by 50%, and (iv) disappearance of the effect upon pulsing the discharge with 2-ms pulses and 1-ms pauses, can be explained by postulating that oxide formation is dominated by negative ions O_m^- ($1 \leq m \leq 3$) accumulating in the gas as it travels through the plasma zone and adsorbing to the oxide surface near the end of the plasma zone, at $y = 0$.

The question if the transport of negative ions from the plasma zone towards the anode might be the dominant step in oxide film formation by low-pressure DC-plasma "anodization" was repeatedly asked in the literature and it was answered negatively. Instead, the supply of atomic oxygen and subsequent attachment of electrons to adsorbed O atoms was concluded to be rate-determining [70, 71]. In the present case, however, the latter mechanism can very likely be excluded, based on the experimental observations (ii) to (iv) reported above.

A final remark should address the question if there are any significant direct electrical effects from the electrical field driving the DBD on the oxidation process. While the applied voltages are three orders of magnitude larger than typical Cabrera–Mott potentials, the large voltage drop across the dielectric wall of the DBD reactor, typically 10^5 to 10^6 times as thick as the oxide film, must be taken into consideration, resulting in negligible potentials at the oxide surface. Experiments, too, show that direct electrical effects of the alternating electric field in the discharge on the oxidation process can be disregarded: See the continuity of $X(y)$ graphs in Fig. 6 across the DBD/PoD boundary in case of 100 ppm O_2 or 20 ppm O_2 in Ar with 1% Xe added.

Conclusions

Oxide films with thicknesses beyond 5 nm are typically achieved within 15 min at room temperature by exposing aluminum surfaces to dielectric-barrier discharges in highly diluted mixtures of O_2 and argon with oxygen fractions between 20 and 500 ppm. Metal oxidation under these conditions is mainly due to the combined effects of super-bandgap irradiation by high-energy (9.8 eV) photons from the discharge and the presence of substantial number densities of oxygen atoms in the order of 10^{15} cm^{-3}.

In the close pre-discharge zone, oxide growth is found to be entirely due to surface irradiance by photons from the DBD in presence of O_2 and virtually independent of the

fraction of O_2. Oxidation rates are orders of magnitudes larger than what was reported in the literature for photons with sub-bandgap energy (4 eV). There are indications, on the other hand, that 9.8-eV photon irradiation impedes oxide growth beyond a certain thickness, due to the generation of positive space charges in the oxide.

In the remote post-discharge region, oxide growth can be attributed to oxygen atoms with number densities in the order of 10^{14} cm^{-3} while, on the studied time scale, effects of metastable ozone are negligible. Here, the analysis in terms of Cabrera–Mott (CM) theory results in CM potentials between -1.5 and -2.1 V.

While oxidation by VUV photons and/or oxygen atoms generally ceases at a critical thickness between 5 and 6 nm, much thicker oxide films of up to 18 nm can be achieved within 40 min under suitable conditions, in the rear zone of the DBD, without cessation of the process at a critical thickness within a process duration of 10,000 s. Experiments lead to conclude that this oxide growth mode is due to negative ions O_m^- ($1 \leq m \leq 3$) accumulating in the downstream region of the DBD.

Experiments show that direct electrical effects of the alternating electric field in the discharge on the oxidation process can be disregarded which is to be expected in view of the large voltage drop across the dielectric wall of the DBD reactor, typically 10^5 to 10^6 times as thick as the oxide film.

Declarations

Competing interests I, CPK, declare that the authors have no competing interests of financial or personal nature, or other interests that might be perceived to influence the results and/or discussion reported in this paper.

References

1. Ramírez LP, Bournel F, Gallet JJ, Dudy L, Rochet F (2022) J Phys Chem C 126:2517. https://doi.org/10.1021/acs.jpcc.1c09388

2. Gorobez J, Maack B, Nilius N (2021) Phys Stat Sol B 258:2000559. https://doi.org/10.1002/pssb.202000559
3. Laboureur D, Glabeke G, Gouriet JB (2021) J Nanopart Res 23:71. https://doi.org/10.1007/s11051-021-05170-z
4. Stilhano Vilas Boas CR, Sturm JM, van den Beld WTE, Bijkerk F (2021) Materialia 20:101203. https://doi.org/10.1016/j.mtla.2021.101203
5. Geiger M, Hagel M, Reindl T, Weis J, Weitz RT, Solodenko H, Schmitz G, Zschieschang U, Klauk H, Acharya R (2021) Sci Rep 11:6382. https://doi.org/10.1038/s41598-021-85517-7
6. Murray CE (2021) Mater Sci Eng R Rep 146:100646. https://doi.org/10.1016/j.mser.2021.100646
7. Hickmott TW (2019) J Appl Phys 125:025305. https://doi.org/10.1063/1.5024665
8. Jeurgens LPH, Sloof WG, Tichelaar FD, Mittemeijer EJ (2002) J Appl Phys 92:1649. https://doi.org/10.1063/1.1491591
9. Hass G (1974) Z Anorg Chem 254:96
10. Evertsson J, Bertram F, Zhang F, Rullik L, Merte LR, Shipilin M, Soldemo M, Ahmadi S, Vinogradov N, Carlà F, Weissenrieder J, Göthelid M, Pan J, Mikkelsen A, Nilsson JO, Lundgren E (2015) Appl Surf Sci 349:826. https://doi.org/10.1016/j.apsusc.2015.05.043
11. Cai N, Zhou G, Müller K, Starr DE (2011) Phys Rev Lett 107:035502. https://doi.org/10.1103/PhysRevLett.107.035502
12. Grimblot J, Eldridge JM (1982) J Electrochem Soc 129:2369. https://doi.org/10.1149/1.2123529
13. Cabrera N, Mott NF (1949) Rep Prog Phys 1949:163. https://doi.org/10.1088/0034-4885/12/1/308
14. Guise O, Levy J, Yates JT Jr (2001) Thin Solid Films 496:426. https://doi.org/10.1016/j.tsf.2005.08.358
15. Reichel F, Jeurgens LPH, Mittemeijer EJ (2008) Acta Mater 56:2897. https://doi.org/10.1016/j.actamat.2008.02.031
16. Starodub D, Gustafsson T, Garfunkel E (2004) Surf Sci 552:199. https://doi.org/10.1016/j.susc.2004.01.019
17. Fehlner FP (1986) Low-temperature oxidation—the role of vitreous oxides. John Wiley & Sons, New York
18. Davies JA, Domeij B, Pringle JPS, Brown F (1965) J Electrochem Soc 112:675. https://doi.org/10.1149/1.2423662
19. Shapiro S (1963) Phys Rev Lett 11:80. https://doi.org/10.1103/PhysRevLett.11.80
20. Miles JL, Smith PH (1963) J Electrochem Soc 110:1240. https://doi.org/10.1149/1.2425633
21. Halverson DE, Cocke DL (1987) Thin Solid Films 155:133. https://doi.org/10.1016/0040-6090(87)90459-7
22. Baier-Saip JA, Avila JI, Tarrach G, Cabrera AL, Fuenzalida V, Zarate RA, Schuller IK (2005) Surf Coat Technol 195:168. https://doi.org/10.1016/j.surfcoat.2004.06.020
23. Behnke JF, Steffen H, Sonnenfeld A, Foest R, Lebedev V, Hippler R (2002) Proc. Hakone 8: Int. Symp. on High Pressure, Low Temperature Plasma Chemistry, Tartu, Estonia
24. Knechten K, LeClair P, Kohlhepp JT, Swagten HJM, Koopmans B, de Jonge WJM (2001) J Appl Phys 90:1675. https://doi.org/10.1063/1.1379046
25. Knechten K, Kniknie BJ, Engeln R, Swagten HJM, Koopmans B, van de Sanden MCM, de Jonge WJM (2004) J Vac Sci Technol A 22:L11. https://doi.org/10.1116/1.1807837
26. Quade A, Wulff H, Steffen H, Tun TM, Hippler R (2000) Thin Solid Films 377–378:626. https://doi.org/10.1016/S0040-6090(00)01474-7
27. Rider AN, Lamb RN, Koch MH (2001) Surf Interface Anal 31:302. https://doi.org/10.1002/sia.978
28. Strohmeier BR (1990) Surf Interface Anal 15:51. https://doi.org/10.1002/sia.740150109
29. Alexander MR, Thompson GE, Zhou X, Beamson N, Fairley N (2002) Surf Interface Anal 34:485. https://doi.org/10.1002/sia.1344
30. Jablonski A, Powell CJ (2020) J Phys Chem Ref Data 49:033102. https://doi.org/10.1063/5.0008576
31. Shinotsuka H, Tanuma S, Powell CJ, Penn DR (2015) Surf Interface Anal 47:871. https://doi.org/10.1002/sia.5789
32. Shinotsuka H, Tanuma S, Powell CJ, Penn DR (2019) Surf Interface Anal 51:427. https://doi.org/10.1002/sia.6598
33. Jablonski A, Salvat F, Powell CJ, Lee AY (2016) NIST Electron Elastic-Scattering Cross-Section Database Version 4.0, NIST Standard Reference Database Number 64, National Institute of Standards and Technology, Gaithersburg MD, 20899, USA. https://srdata.nist.gov/srd64/Transport (retrieved February 2, 2022)
34. Wäckelgård E (1996) J Phys: Condens Matter 8:4289. https://doi.org/10.1088/0953-8984/8/23/019
35. Chabal YJ (1988) Surf Sci Rep 8:211. https://doi.org/10.1016/0167-5729(88)90011-8
36. Moine B, Bizarri G, Varrel B, Rivoire J-Y (2007) Opt Mater 29:1148. https://doi.org/10.1016/j.optmat.2006.05.004

37. Klages CP, Bröcker L, Betz ML, Raev V (2023) Plasma Chem Plasma Process 43:285. https://doi.org/10.1007/s11090-022-10293-9
38. Kogelschatz U, Eliasson B, Egli W (1997) J Phys IV France 7:C4-47. https://doi.org/10.1051/jp4:1997405
39. Klages CP, Czerny AK, Philipp J, Becker MM, Loffhagen D (2017) Plasma Process Polym 14:1700081. https://doi.org/10.1002/ppap.201700081
40. Pitchford LC, Alves LL, Bartschat K, Biagi SF, Bordage MC, Phelps AV, Ferreira CM, Hagelaar GJM, Morgan WL, Pancheshnyi S, Puech V, Stauffer A, Zatsarinny O (2013) J Phys D: Appl Phys 46:334001. https://doi.org/10.1088/0022-3727/46/33/334001
41. Velazco JE, Kolts JH, Setser DW (1978) J Chem Phys 69:4357. https://doi.org/10.1063/1.436447
42. Oka T, Kogoma M, Imamura M, Arai S, Watanabe T (1979) J Chem Phys 70:3384. https://doi.org/10.1063/1.437923
43. Keto JW, Hart CF, Kuo C-Y (1981) J Chem Phys 74:4450. https://doi.org/10.1063/1.441687
44. Brunet H, Birot A, Dijols H, Galy J, Millet P, Salamero Y (1982) J Phys B At Mol Phys 15:2945
45. Ghez R (1973) J Chem Phys 58:1838. https://doi.org/10.1063/1.1679440
46. Burstein GT, Davenport AJ (1989) J Electrochem Soc 136:936. https://doi.org/10.1149/1.2096890
47. Cabrera N, Terrien J, Hamon J (1947) Comptes Rendus Acad Sci Paris 224:1558
48. Cabrera N (1949) Phil Mag 40:175. https://doi.org/10.1080/14786444908521716
49. Ramanathan S, Chi D, McIntyre PC, Wetteland CJ, Tesmer JR (2003) J Electrochem Soc 150:F110. https://doi.org/10.1149/1.1566416
50. Chang CL, Ramanathan S (2007) J Electrochem Soc 154:G160. https://doi.org/10.1149/1.2737347
51. Fromhold Jr AT (1975) Theory of metal oxidation, Vol. 1: Fundamentals, North-Holland Publishing Company, Amsterdam
52. Chang CL, Engelhard MH, Ramanathan S (2008) Appl Phys Lett 92:263103. https://doi.org/10.1063/1.2952282
53. Chang CL, Sankaranarayanan SKRS, Engelhard MH, Shutthanandan V, Ramanathan S (2009) J Phys Chem C 113:3502. https://doi.org/10.1021/jp808424g
54. Yolles RS, Wise H (1968) J Chem Phys 48:5109. https://doi.org/10.1063/1.1668181
55. Betz, ML (2022) unpublished
56. Golda J, Biskup B, Layes V, Winzer T, Benedikt J (2020) Plasma Process Polym 17:e1900216. https://doi.org/10.1002/ppap.201900216
57. Heays AN, Bosman AD, van Dishoec EF (2017) A&A 602:A105. https://doi.org/10.1051/0004-6361/201628742
58. Pong W (1969) J Appl Phys 40:1733. https://doi.org/10.1063/1.1657840
59. Afanas'ev VV (2014) Internal Photoemission Spectroscopy. Elsevier Ltd., Amsterdam
60. French RH (1990) J Am Ceram Soc 13:471. https://doi.org/10.1111/j.1151-2916.1990.tb06541.x
61. Huang Z, Messina DC, Eller BS (2021) J Vac Sci Technol A 39:042402. https://doi.org/10.1116/6.0001010
62. Smith DY, Shiles E, Inokuti M (1997) in: Handbook of Optical Constants of Solids 1:369. https://doi.org/10.1016/B978-012544415-6.50016-9
63. Daniel Franta D, David Nečas D, Ivan Ohlídal I, Jiří Jankuj J (2015) Proc. SPIE 9628, optical systems design 2015: optical fabrication, testing, and metrology V, 96280F (24 September 2015). http://dx.doi.org/https://doi.org/10.1117/12.2190109, data file available at http://newad.physics.muni.cz/table-udm/Al2O3-X2890-SPIE9628.Enk
64. Fromhold AT Jr (1979) Oxid Met 13:475. https://doi.org/10.1007/BF00605111
65. Powell RJ (1976) Appl Phys Lett 28:643. https://doi.org/10.1063/1.88607
66. Lauer JL, Shohet JL, Cismaru C, Hansen RW, Foo MY, Henn TJ (2002) J Appl Phys 91:1242. https://doi.org/10.1063/1.1428790
67. Betz M, Bröcker L, Jung A, Raev V, Bandorf R, Gerdes H, Klages CP (2023) International Symposium on Plasma Chemistry (ISPC25), Kyoto, Japan
68. Fromm E (1998) Kinetics of metal-gas interactions at low temperatures, Ertl G (Ed), Springer Series in Surface Sciences 36, Springer, Berlin
69. Litrico G, Proulx P, Gouriet J-B, Rambaud P (2015) Adv Powd Technol 26:1. https://doi.org/10.1016/j.apt.2014.11.004
70. Olive G, Pulfrey DL, Young L (1972) Thin Solid Films 12:427. https://doi.org/10.1016/0040-6090(72)90107-1
71. Matsumura K (1989) J Appl Phys 65:1866. https://doi.org/10.1063/1.342921

Springer